Physics of Fluids

# High-Schmidt-number mass transport mechanisms from a turbulent flow to absorbing sediments

Cite as: Phys. Fluids **24**, 085103 (2012); https://doi.org/10.1063/1.4739064
Submitted: 05 February 2012 . Accepted: 28 June 2012 . Published Online: 06 August 2012

Carlo Scalo, Ugo Piomelli, and Leon Boegman

View Online

Export Citation

ARTICLES YOU MAY BE INTERESTED IN

Large-eddy simulation of high-Schmidt number mass transfer in a turbulent channel flow
Physics of Fluids **9**, 438 (1997); https://doi.org/10.1063/1.869138

Near-wall passive scalar transport at high Prandtl numbers
Physics of Fluids **19**, 065105 (2007); https://doi.org/10.1063/1.2739402

Direct numerical simulation of turbulent channel flow up to $\mathrm{Re}_\tau = 590$
Physics of Fluids **11**, 943 (1999); https://doi.org/10.1063/1.869966

AIP Publishing



© 2012 American Institute of Physics.

# High-Schmidt-number mass transport mechanisms from a turbulent flow to absorbing sediments

Carlo Scalo,[1,a)] Ugo Piomelli,[1,b)] and Leon Boegman[2,c)]
[1]*Department of Mechanical and Materials Engineering, Queen's University, 130 Stuart Street, Kingston, Ontario, Canada, K7L 3N6*
[2]*Department of Civil Engineering, Queen's University, 58 University Avenue, Kingston, Ontario, Canada, K7L 3N6*

(Received 5 February 2012; accepted 28 June 2012; published online 6 August 2012)

We have investigated the mechanisms involved in dissolved oxygen (DO) transfer from a turbulent flow to an underlying organic sediment bed populated with DO-absorbing bacteria. Our numerical study relies on a previously developed and tested computational tool that couples a bio-geochemical model for the sediment layer and large-eddy simulation for transport on the water side. Simulations have been carried out in an open channel configuration for different Reynolds numbers ($Re_\tau = 180$–$1000$), Schmidt numbers ($Sc = 400$–$1000$), and bacterial populations ($\chi^* = 100$–$700\ \mathrm{mg\ l^{-1}}$). We show that the average oxygen flux across the sediment-water interface (SWI) changes with $Re_\tau$ and $Sc$, in good agreement with classic heat-and-mass-transfer parametrizations. Time correlations at the SWI show that intermittent peaks in the wall-shear stress initiate the mass transfer and modulate its distribution in space and time. The diffusive sublayer acts as a de-noising filter with respect to the overlying turbulence; the instantaneous mass flux is not affected by low-amplitude background fluctuations in the wall-shear stress but, on the other hand, it is receptive to energetic and coherent near-wall transport events, in agreement with the surface renewal theory. The three transport processes involved in DO depletion (turbulent transport, molecular transport across the diffusive sublayer, and absorption in the organic sediment layer) exhibit distinct temporal and spatial scales. The rapidly evolving near-wall high-speed streaks transport patches of fluid to the edge of the diffusive sublayer, leaving slowly regenerating elongated patches of positive DO concentration fluctuations and mass flux at the SWI. The sediment surface retains the signature of the overlying turbulent transport over long time scales, allowed by the slow bacterial absorption. © *2012 American Institute of Physics*. [http://dx.doi.org/10.1063/1.4739064]

## I. INTRODUCTION

The prediction of dissolved oxygen (DO) levels is critical for preserving and monitoring marine ecosystems. Oxygen evolves in water bodies as a high-Schmidt-number passive scalar with saturation levels highly dependent on temperature. It is entrained at the surface and transported across the water column by the turbulent motions. Many natural factors can interfere with this mixing process, such as stratification, which damps the turbulent motion, reducing the supply of oxygen to the near-bed region where decomposition of organic matter in the sediment layer by oxygen-consuming bacteria can cause DO concentration to drop to unsustainable levels for aquatic life; anoxic "dead zones" are then formed, with considerable economical and environmental impacts. The characterization of the physical processes involved in this problem is twofold: (i) the governing mechanisms in

a)cscalo.ca@gmail.com.
b)ugo@me.queensu.ca.
c)leon.boegman@civil.queensu.ca.

 © 2012 American Institute of Physics

high-Schmidt-number mass transfer from a turbulent flow to a solid boundary need to be identified and the adequacy of currently adopted models assessed; (ii) the transport in the sediment layer (bio-geochemical characterization) and its interaction with the overlying turbulent field need to be modeled.

The mechanisms of high-Schmidt-number mass transfer from a turbulent flow to a solid boundary involve many fundamental aspects of near-wall turbulence, such as the interaction between the viscous sublayer and buffer-layer events.[1,2] Einstein and Li[3] were perhaps the first to propose a one-dimensional model describing the cyclic growth (slow development and abrupt breakdown) of the viscous sublayer. The effects of the unsteadiness of the viscous sublayer on high-Schmidt-number mass-transfer mechanisms was subsequently investigated by Hanratty[4] who proposed a similar one-dimensional model for the unsteady growth of the diffusive sublayer: the near-wall region is pictured as a series of periodically renewing patches of fluid transporting the free-stream concentration value, stagnating at the wall (where molecular mass transfer occurs) and then being ejected to the outer region. This was the seminal idea of what is more recently referred to as the "surface renewal theory."[5] Reiss and Hanratty[6] extended this work by directly measuring the instantaneous mass-transfer rate to a solid boundary and relating it to the overlying fluctuating velocity field. Their results highlight the role of velocity fluctuations remaining active in the lowest layers of the viscous sublayer. Sirkar and Hanratty[7] carried out experiments at $Sc = 2300$, which supported the correlation between the instantaneous mass flux and the low frequency spanwise velocity fluctuations persisting in the viscous sublayer. Also, streamwise velocity fluctuations were claimed not to be effective in controlling the mass transfer and are neglected in their transport model. Pinczewski and Sideman[8] extended the model of Hanratty[4] to a concentration boundary layer developing both in space and time, being renewed by quasi-periodic bursting events. A parametrization in closed form is obtained relating the average mass transfer to the mean wall-shear stress and $Sc$. The emphasis, in their work, is on the Schmidt number effects: as $Sc$ increases, the diffusive sublayer layer acts as a progressively stronger limiting layer for the mass transfer; only a fraction of the eddies (the most energetic ones) successfully modulate the diffusive sublayer thickness, and, therefore, the mass flux. Shaw and Hanratty[9] pointed out the strong similarity between the spatial distribution of the overlying streamwise-oriented vortices and the mass flux at the wall, which evolves over longer time-scales. Time spectra of mass-transfer fluctuations are shown to scale with $Sc$. Previous studies from the same group[7,10] confirm the reduced transverse spatial extent of the mass flux distribution at the wall with respect to the overlying turbulent structures. Investigations of high-Schmidt-number mass transfer to a pipe wall were carried out by Campbell and Hanratty[11] stressing the strong relation between the low-pass filtered transverse velocity gradient fluctuations at the wall and the corresponding concentration fluctuations, in line with Sirkar and Hanratty.[7] In conclusion it is established that mass transfer is controlled by the low frequency component of the velocity fluctuations in quasi-streamwise vortices and that the diffusive sublayer acts as a low-pass filter. The same authors, in a separate work,[12] confirm this picture with a non-linear numerical model for the diffusive sublayer forced by experimentally extracted velocity data. All indications support the idea that mass transfer at the wall is not controlled by the most energetic velocity fluctuations,[13] but it is instead dominated by the low-frequency component of the velocity field and that, as $Sc$ increases, progressively fewer turbulent transport events reach the thinner diffusive sublayer and, therefore, govern the mass transfer.

The aforementioned experimental investigations come with numerous challenges. Measurement of the very small length scales and time scales of the scalar field represents, perhaps, the most severe one. Moreover, in the case of oxygen concentration measurements, involving both the fluid side and the sediment layer, the presence of an interface between two media can cause measurement difficulties.[14,15] Numerical investigations have analogous difficulties. Accuracy can be an issue, as high-Schmidt-number passive scalar exhibits a range of sub-Kolmogorov scales extending as far as the Batchelor scale $\eta_B = \eta/\sqrt{Sc}$, where $\eta$ is the Kolmogorov length scale; resolving the complete range of scales can become an unfeasible option. When modelling unresolved scales, establishing the adequacy of grid resolution can, therefore, be problematic. These issues have been addressed by several researchers in the past. The suitability of large-eddy simulation (LES) for investigating high-Schmidt-number mass transfer was first tested by Calmet and Magnaudet[16] and later by Dong *et al.*[17] Their results confirmed the suitability of LES in predicting, with very good

accuracy, the essential characteristics of a high-Schmidt-number scalar field such as the mass flux at the solid wall. A hybrid approach has been adopted by Bergant and Tiselj[18] who performed direct numerical simulation (DNS) of the velocity field with a LES-like formulation for the scalar field up to $Re_\tau = 400$ and $Sc = 200$. They showed that low-order statistics (including turbulent fluxes) are captured very accurately even on coarse grids (as also confirmed by the grid convergence tests in Scalo *et al.*[19]) and that spectra and scalar variance profiles in the diffusive sublayer and concentration buffer layer ($y^+ < 5$) are unaffected by the grid cutoff of sub-Kolmogorov scales. Schwertfirm and Manhart[20] performed a fully resolved DNS at $Re_\tau = 180$ up to $Sc = 49$ by adopting a hierarchical grid approach. A scaling law for the mass-transfer coefficient with $Sc$ is derived and compared with classic experimental correlations. More recently, Hasegawa and Kasagi[21] adopted a similar numerical approach to perform simulations up to $Sc = 400$ at $Re_\tau = 150$. With the aid of the generated data, a one-dimensional linear model has been derived reproducing the frequency response of the fluctuating mass-transfer rate at the wall to the overlying turbulent velocity fluctuations.

All of the previously mentioned work focused on aspects of high-Schmidt-number mass-transfer exclusively connected to turbulence. However, the presence of a porous and mass-absorbing sediment layer, in the case of oxygen transport, raises questions as to how turbulence interacts with it. In the sediment, solutes dissolved in the pore water, in general, diffuse through the porous medium (at a slower rate than in pure water), disperse and are advected by interstitial flow (typically modeled by Darcy's Law for low permeabilities). In the case of dissolved oxygen in marine environments absorption by bacterial decomposition may also occur.[5] However, for flat and cohesive beds the dominant processes are diffusion and absorption.[19] Advection becomes particularly important in presence of large-scale bed roughness where persistent pressure differences at the sediment-water interface (SWI) drive a mean interstitial current that transports fluid and solutes in and out of the underlying bed.[5] Dispersion effects are important for highly permeable sediment beds and, such as advection, are driven by pore water flow. A thorough discussion on the effects of dispersion and advection in the sediment layer and the associated modelling problematics can be found in Scalo *et al.*[19] and several works by Higashino and co-workers.[22–26]

In the present work, we adopt the model developed by Scalo *et al.*[19] to study the turbulence-driven small-scale transport processes involved in oxygen transfer to smooth and cohesive organic sediment layers (with no dispersion or advection effects) and their sensitivity to the governing parameters such as $Re_\tau$, $Sc$, and $\chi^*$ (oxygen absorbing bacterial population density). The present work is the natural extension of previous experimental,[15] numerical,[22] and field-scale[27] studies to a numerical investigation based on an eddy resolving method. In the following we begin by describing the complete transport model and the problem setup. Results are then presented for all cases investigated showing first-order statistics and temporal and spatial correlations at the SWI. A conceptual model for the transport is deduced from the presented data and confirmed by the instantaneous visualizations.

## II. PROBLEM FORMULATION

The filtered conservation equations of mass and momentum can be obtained by applying a filtering operator $\overline{(\,)}$ to the governing equations,[28] resulting in

$$\frac{\partial \overline{u}_i}{\partial x_i} = 0, \tag{1}$$

$$\frac{\partial \overline{u}_j}{\partial t} + \frac{\partial \overline{u}_i \overline{u}_j}{\partial x_i} = -\frac{\partial \overline{p}}{\partial x_j} - \frac{\partial \tau_{ij}}{\partial x_i} + \frac{1}{Re_b}\nabla^2 \overline{u}_j - f\delta_{1j}, \tag{2}$$

where $x_1$, $x_2$, and $x_3$ (or $x$, $y$, and $z$) are, respectively, the streamwise, wall-normal and spanwise directions, and $\overline{u}_i$ the filtered velocity components in those directions. These equations have been

made dimensionless by using $\delta$ (height of the open channel) as reference length scale, and $U_b$ (the volume average streamwise velocity component) as velocity scale. The bulk Reynolds number is $Re_b = U_b\delta/\nu$; where $\nu$ is the kinematic viscosity of water. The forcing term $f$ in the streamwise momentum equation represents the normalized mean pressure gradient driving the flow. The sub-grid scale (SGS) stresses are modeled using the dynamic procedure.[29,30]

Oxygen dissolved in water behaves like a passive scalar with very low molecular diffusivity, $D$, compared to the kinematic viscosity. The filtered transport equation for DO is, therefore,

$$\frac{\partial \overline{c}}{\partial t} + \frac{\partial \overline{u}_i \overline{c}}{\partial x_i} = \frac{\partial}{\partial x_i}\left[\frac{1}{Sc\, Re_b}\frac{\partial \overline{c}}{\partial x_i} - J_i^{sgs}\right], \tag{3}$$

where $Sc = \nu/D$ is the Schmidt number and $\overline{c}$ is the instantaneous filtered scalar concentration field normalized with the freestream DO concentration $C^*_\infty$. The SGS scalar flux, $J_i^{sgs}$, is also modeled with the same approach used for the velocity field.

The normalized instantaneous DO concentration in the sediment layer, $c_s$, is determined by more complex mechanisms. Dissolved oxygen is diffused but also depleted by decomposing organic matter. The present investigation will focus on smooth and cohesive sediment beds (low porosities), where pore-water-flow driven advection and dispersion effects can be neglected.[19] The momentum and mass (DO) exchange across the SWI will, therefore, be exclusively molecular. The governing equation for $c_s$ is

$$\frac{\partial c_s}{\partial t} = \frac{\partial}{\partial x_i}\left[\frac{F(\varphi)}{Sc\, Re_b}\frac{\partial c_s}{\partial x_i}\right] - \dot{c_s}, \tag{4}$$

where $F(\varphi)$ is a function of the sediment porosity $\varphi$ which accounts for the reduction of the molecular diffusivity due to porosity and tortuosity. A commonly used approximation in the field for this function is $F(\varphi) = \varphi^2$ (valid for $\varphi < 0.7$).[25] It is possible to retrieve the value of the sediment porosity from the measurable slope discontinuity in the mean oxygen profiles at the SWI by imposing the continuity of the mass flux from both sides of the SWI.[14] The DO absorption by organic matter is represented by the sink term, $\dot{c_s}$, which must be modeled. The parametrization for the non-linear sink term, $\dot{c}_s$, due to Higashino *et al.*,[22] is

$$\dot{c}_s = \chi \frac{c_s}{K_{O_2} + c_s}, \tag{5}$$

where

$$\chi = \frac{\chi^* \mu^*_\chi}{Y_c}\frac{\delta}{U_b\, C^*_\infty} \tag{6}$$

and

$$K_{O_2} = \frac{K^*_{O_2}}{C^*_\infty}. \tag{7}$$

The parameters used in (6) and (7) are $\mu^*_\chi$, maximum specific DO utilization rate (in day$^{-1}$), $K^*_{O_2}$, half-saturation coefficient for DO utilization (in mg l$^{-1}$), $Y_c$ effective yield for the microbial utilization of DO and $\chi$*, biomass concentration of oxygen absorbing organisms (currently not directly measurable). The values for these constants suggested by Higashino *et al.*[22] and Scalo *et al.*[19] are shown in Table I. We assume a constant and uniform value of $\chi$* within the sediment layer.

TABLE I. Bio-geochemical parameters for oxygen absorption model (5).

| $\mu^*_\chi$ | $K^*_{O_2}$ | $Y_c$ | $\chi^*$ |
|---|---|---|---|
| 2.4 day$^{-1}$ | 0.2 mg l$^{-1}$ | 1 mg$_\chi$/mg$_{DO}$ | 100–700 mg l$^{-1}$ |

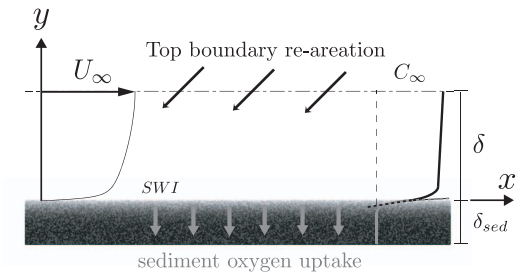


FIG. 1. Computational setup. The diffusive sublayer thickness is exaggerated for visualization purposes. The value of oxygen concentration in the bulk flow is kept at $C_\infty$ by re-areation from the top-boundary.

## III. COMPUTATIONAL SETUP

The computational setup used is shown in Figure 1. The flow is driven by a uniform pressure gradient $f$ dynamically adjusted in order to achieve the desired flow rate. The governing equations (1), (2), and (3) are solved in a Cartesian domain. In the streamwise and spanwise directions, $x$ and $z$, periodic boundary conditions are used for all quantities. The velocity obeys no-slip conditions at the lower wall, and, at the top boundary, free-slip conditions; for the scalar field we use Neumann conditions at the SWI with a flux that varies in space and time obtained by solving the sediment layer transport equation (4). Further details regarding the numerical strategy adopted for the coupling between the sediment layer and the water side and comparison with experiments can be found in Scalo *et al.*[19] The oxygen dynamically absorbed by the sediment layer across the SWI is re-inserted in the flow, at the same rate, from the top boundary by means of an imposed instantaneous flux. The value of the volume averaged DO concentration is maintained constant and equal to the initial value.

The numerical model used to compute the flow on the water side is a well-validated finite-difference code,[31] based on a staggered grid. Second-order central differences are used for both convective and diffusive terms. A Crank-Nicolson scheme is used for the wall-normal diffusive term, and a low-storage third-order Runge-Kutta method for the other terms. The solution of the Poisson equation is obtained by Fourier transform of the equation in the spanwise and streamwise directions, followed by a direct solution of the resulting tridiagonal matrix, at each wavenumber. The code is parallelized using the Message Passing Interface (MPI) protocol. The equations in the sediment layer are solved with the same numerical approach as adopted for the water side and have the same accuracy and stability properties.

We performed numerical simulations of an open channel flow by adjusting the forcing term in (2) in order to obtain four different friction Reynolds numbers $Re_\tau = 180, 400, 620$, and 1000. This resulted in four velocity fields each simultaneously transporting 6 scalar fields, one for every combination of three Schmidt numbers, $Sc = 400$, 690, 1020 (corresponding to water temperatures of 25 °C, 15 °C, and 8 °C and to dissolved oxygen saturation levels of $C^*_\infty \simeq 8.3$, 10.1, and 12 mg $l^{-1}$), and two bacterial populations, $\chi^* = 100$ and 700 mg $l^{-1}$ (Table II). A porosity of $\varphi = 0.55$ has been used for all cases. The domain size has been chosen in order to accommodate the large structures; the near-wall streaks and the elongated concentration patches at the SWI (shown

TABLE II. Simulation parameters.

| Type | $Re_b$ | $Re_\tau$ | $L_x \times L_y \times L_z$ | $N_x \times N_y \times N_z$ | $\Delta x^+$ | $\Delta z^+$ | $\Delta y^+$ | $Sc$ |
|---|---|---|---|---|---|---|---|---|
| Hybrid | 2800 | 180 | $32 \times 1 \times 7$ | $1024 \times 192 \times 384$ | 5.6 | 3.3 | 0.055–2.5 | 400, 690, 1020 |
| Hybrid | 6900 | 400 | $14 \times 1 \times 3$ | $1024 \times 192 \times 384$ | 5.5 | 3.1 | 0.052–6.5 | 400, 690, 1020 |
| LES | 11500 | 620 | $14 \times 1 \times 3$ | $384 \times 256 \times 192$ | 23 | 9.6 | 0.061–7.3 | 400, 690, 1020 |
| LES | 19500 | 1000 | $14 \times 1 \times 3$ | $512 \times 384 \times 256$ | 27 | 12 | 0.060–8.3 | 400, 690, 1020 |

later). The grid size has been chosen accordingly to keep the resolution at a DNS level ($\Delta x^+ \simeq 5$ and $\Delta z^+ \simeq 3$) for the velocity field for cases $Re_\tau = 180$ and 400 and (very fine) LES resolution ($\Delta x^+ \simeq 23$ and $\Delta z^+ \simeq 10$) for cases $Re_\tau = 620$ and 1000. The sub-grid scale closure is therefore used, for the velocity field, only for the higher Reynolds number cases. The coarsest resolution adopted here accurately describes the concentration field as shown by Scalo *et al.*[19] and by Calmet and Magnaudet.[16] The hybrid approach used for the finer simulations is similar to one proposed by Bergant and Tiselj,[18] which guarantees a very accurate description of the concentration field in the near-wall region. The resolution in the wall-normal direction has been chosen, for every Reynolds number, based on the expected diffusive sublayer thickness at $Sc = 1020$. In all cases the sediment layer depth is fixed to $\delta_{sed} = 0.3\delta$ (see Figure 1) and discretized with 65 grid points. The sediment layer shares the same spanwise and streamwise resolution of the water side as well as the wall-normal resolution at the SWI.

The adopted physical parameters cover a wide range of fluid dynamic conditions bracketing the ones covered by the experimental investigations by O'Connor and Hondzo[15] (reproduced by Scalo *et al.*[19]). These were focused on a higher temperature range, $T = 26\ ^\circ$C–$37\ ^\circ$C—unphysical for the near-bed regions of lakes and oceans—a smaller range of friction Reynolds numbers, from 241 to 630, and one (calibrated) bacterial population of 700 mg $l^{-1}$ and porosity of $\varphi = 0.55$. The physical height of the open channel in the present simulations corresponds to $\delta = 10$ cm and the bulk velocities are in the range of 3–27 cm s $^{-1}$ (the channel half-width in the recirculating flume experiments by O'Connor and Hondzo[15] is 7.6 cm and bulk velocities in the range 5–11 cm s $^{-1}$). Saturation levels for dissolved oxygen have been used as bulk values used since they are more easily reproducible in lab experiments. However, a change in $C^*_\infty$ (affecting the normalized half-saturation constant (7)) causes only a moderate variation in the numerical solutions due to weak non-linearities in the absorption term (5). A more thorough discussion of the physical relevance of the adopted parameters can be found in Scalo *et al.*[19]

## IV. RESULTS

The discussion of data extracted from the simulations is organized as follows. First, mean profiles of the scalar concentration are shown and the correspondent sediment oxygen uptake is plotted as a function of $Re_\tau$ and $Sc$ and compared to heat-and-mass-transfer laws available in literature (Sec. IV A); then, a statistical analysis of the temporal and spatial structure of the near-wall transport is carried out focusing on auto- and cross-correlation functions between the streamwise component of the wall-shear stress, $\tau_w(x, z; t) = Re_b^{-1}\, \partial u/\partial y$, the DO concentration field at the SWI, $c_{swi}(x, z; t)$, and the instantaneous mass flux across the SWI, $J_{swi}(x, z; t) = (Re_b\, Sc)^{-1} \partial c/\partial y$ (Secs. IV B and IV C); finally, a conceptual model for oxygen depletion is illustrated and instantaneous visualizations are shown to support the global picture arising from the results (Sec. V).

### A. Mean profiles and average mass flux across the sediment-water interface

The mean velocity and concentration profiles in Figure 2 reveal the reduced thickness of the diffusive sublayer with respect to the velocity boundary layer. The oxygen concentration at the SWI increases with $Re_\tau$ and the diffusive sublayer becomes progressively thinner. The most dramatic change in the oxygen distribution occurs from $Re_\tau = 180$ to $Re_\tau = 400$; further increases in the wall-shear stress ($Re_\tau > 400$) result in less evident changes in the DO field, as Reynolds number effects become less significant. This also increases the magnitude of the diffusive flux of oxygen across the SWI and, therefore, the sediment oxygen uptake. The DO penetration depth exhibits a reduced sensitivity to the increasing wall-shear stress; changes in Schmidt number, on the other hand, equally affect both sides of the SWI. Lower $Sc$ result in more intense molecular transport causing, for a given $Re_\tau$, thickening of the diffusive sublayer on the water side and larger penetration depths into the sediment layer. Also, the mean value of oxygen at the SWI decreases for lower $Sc$, as the concentration boundary layer from the water side becomes thicker. Overall, Schmidt number effects are stronger at lower Reynolds numbers.

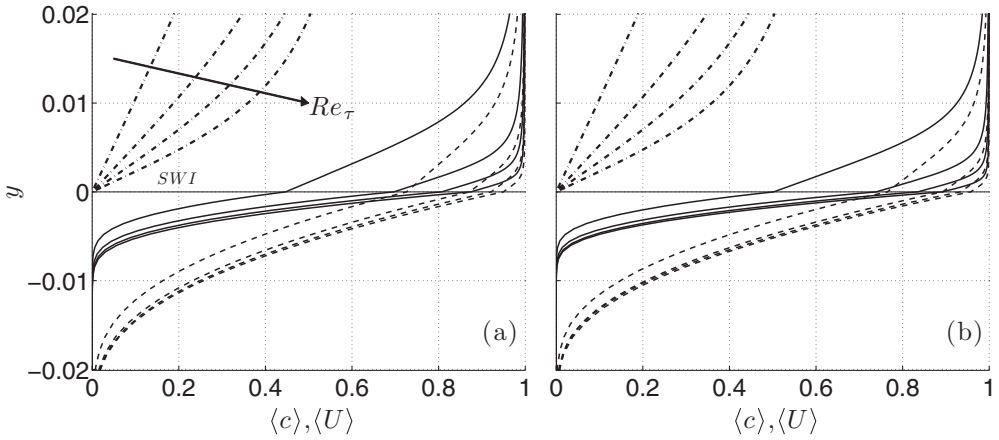


FIG. 2. Mean velocity profiles (— · —) and mean profiles of oxygen concentration for $\chi^* = 700$ mg $l^{-1}$ (———) and $\chi^* = 100$ mg $l^{-1}$ (– – –) for $Re_\tau = 180$, 400, 620, and 1000 (shown by arrow); $Sc = 400$ (a) and $Sc = 1020$ (b).

It is of particular interest in geophysical applications to parametrize the average mass flux $\langle J_{swi} \rangle$ as a function of $Sc$ and $Re_\tau$. A commonly used dimensionless quantity in the field is the Sherwood number[15] defined, in our normalization, as

$$Sh = \frac{Re_b\, Sc}{\Delta C} \langle J_{swi} \rangle \tag{8}$$

with $\Delta C = 1 - \langle c_{swi} \rangle$. As shown in Figure 3 the variation of the Sherwood number with $Re_\tau$ predicted by our LES is not significantly affected by the Schmidt number (the effects of varying the bacterial population, $\chi^*$, are absorbed when normalizing by $\Delta C$); results are in fair agreement with other parametrizations found in heat-and-mass-transfer literature—despite the presence of an organic mass-absorbing sediment layer—such as the one by Shaw and Hanratty[32]

$$K^+ = 0.0889 Sc^{-0.704}, \tag{9}$$

where, in our normalization

$$K^+ = \langle J_{swi} \rangle / u_\tau \Delta C. \tag{10}$$

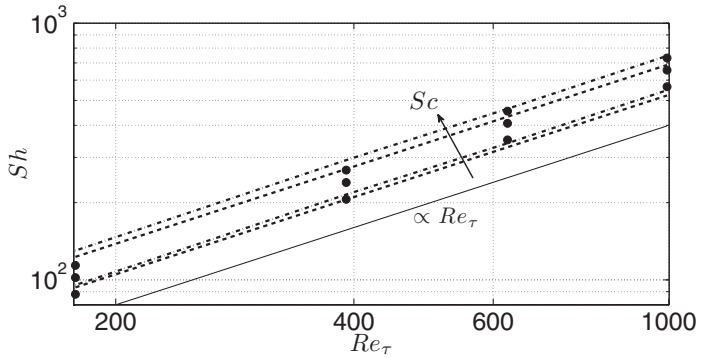


FIG. 3. Sherwood number, $Sh$, as a function of $Re_\tau$ and $Sc$; oxygen flux at the sediment-water interface for all cases in Table II (•), correlation (9) by Shaw and Hanratty[32] (– – –) and correlation (11) by Pinczewski and Sideman[8] (— · —) for $Sc = 400$ and $Sc = 1020$. The trend with $Sc$ is shown for all data by the arrow, the effects of the bacterial population, $\chi^*$, are absorbed via the normalization with $\Delta C$ (8), (10).

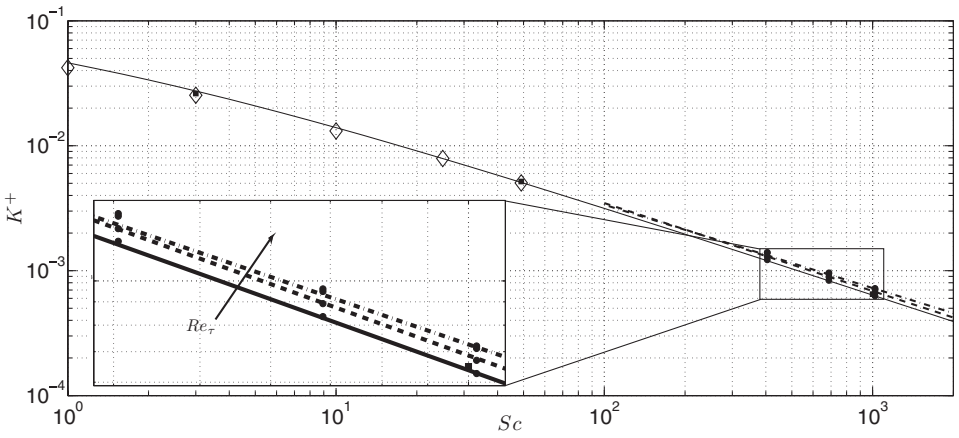


FIG. 4. $K^+$ as a function of $Sc$ and $Re_\tau$; oxygen flux at the sediment-water interface for all cases in Table II (•), correlation (9) by Shaw and Hanratty[32] (– – –), correlation proposed by Schwertfirm and Manhart[20] (———) fitted from their DNS data at $Re_\tau = 180$ and $Sc = 1, 3, 10, 25, 49$ (◇), companion LES at $Sc = 3, 49, 1000$ (■), correlation (11) by Pinczewski and Sideman[8] (— · —).

Good agreement is also found with the semi-analytical model suggested by Pinczewski and Sideman[8]

$$Sh = 0.0102\, Re_b^{9/10}\, Sc^{1/3}. \tag{11}$$

The sediment oxygen uptake, measured by the Sherwood number, increases super-linearly with respect to $Re_\tau$. The agreement is not as satisfactory when results are compared to similar semi-empirical models such as the one suggested by O'Connor and Hondzo.[15]

The same data in Figure 3 is recast in terms of $K^+$ and plotted in Figure 4 together with a correlation proposed by Schwertfirm and Manhart,[20] derived by fitting their (full) DNS data for $Sc = 1, 3, 10, 25, 49$ at $Re_\tau = 180$, and companion LES simulations (with the same computational setup, no sediment layer) at $\Delta x^+ = 12$, $\Delta z^+ = 6$, where the sub-grid scale model is retained for both the velocity and the scalar field. The agreement between DNS results and LES for $Sc = 3$ and 49 is remarkable. Very good agreement is also found between the mass flux predicted by the LES at $Sc = 1000$ and the aforementioned correlation. The DO flux to the sediment shows a clear trend with $Re_\tau$, on the $K^+$ vs $Sc$ plane, as highlighted by the inset image and is in good agreement with the correlations (9) and (11).

Further discussions on the parametrization of the mass flux across the SWI are out of the scope of the present work which is primarily focused on the study of the near-wall (water-side) transport dynamics involved in oxygen depletion, carried out in the remainder of the paper. Future investigations introducing the bed's intrinsic permeability, $K^*$, and porosity as a new parameters,[5] will require the effects of dispersion and advection in the sediment layer to be adequately coupled with eddy-resolving models. This will only be possible after the associated modelling problematics raised by Scalo *et al.*[19] (in particular for the case of oxygen depletion, and in general, for the case of solute transport across the SWI) have been addressed both experimentally and numerically.

### B. The temporal structure of the near-wall transport

The time series in Figure 5 shows the essential mechanisms driving the mass transfer in this problem. Energetic sweeps resulting in peaks in the wall-shear-stress distribution initiate the transport of DO which occurs across the diffusive sublayer and the SWI, from the turbulent core of the channel to the sediment layer. Every strong peak is followed by correspondent increments in the mass flux $J_{swi}$ (integral response) which are delayed in time. The latter causes even smoother increases in the DO level at the SWI, $c_{swi}$, further delayed in time. The mass flux (or, equivalently, the diffusive sublayer thickness) appears to be almost exclusively modulated by the most intense sweeps, penetrating

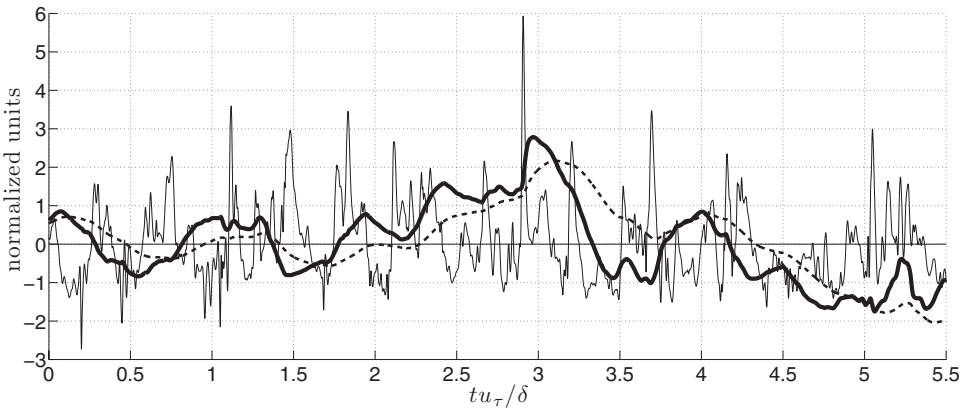


FIG. 5. Time series of instantaneous wall-shear stress, $\tau_w$ (———) (thin solid line), mass flux, $J_{swi}$ (———) (thick solid line), and oxygen concentration, $c_{swi}$ (– – –) at one point on the sediment-water interface, normalized by mean and standard deviation for $Re_\tau = 400$, $\chi^* = 100$ mg l$^{-1}$, $Sc = 400$.

violently across the viscous sublayer, in agreement with Hanratty[4] and Pinczewski and Sideman.[8] The delay between peaks in $J_{swi}$ and peaks in $c_{swi}$ is due to the fact that increments in mass flux at the SWI instantaneously increase the supply of oxygen to the sediment layer, but not its oxygen level. The latter takes some time to increase as mass is transferred across the diffusive sublayer and the interface by molecular transport. Time cross-correlations carried out on the corresponding fluctuating quantities (Figure 6(a))

$$C_1(\tau) = \frac{\langle \tau'_w(x,z;t+\tau) J'_{swi}(x,z;t)\rangle}{\langle \tau'_w J'_{swi}\rangle} \tag{12}$$

$$C_2(\tau) = \frac{\langle J'_{swi}(x,z;t+\tau) c'_{swi}(x,z;t)\rangle}{\langle J'_{swi} c'_{swi}\rangle} \tag{13}$$

allow the quantification of the time shift between the three signals, supporting the cause-and-effect relationship deduced from the time series in Figure 5. The predicted time delay between the mass flux and the wall-shear stress is in very good agreement with the results from the highly resolved simulations by Hasegawa and Kasagi.[21]

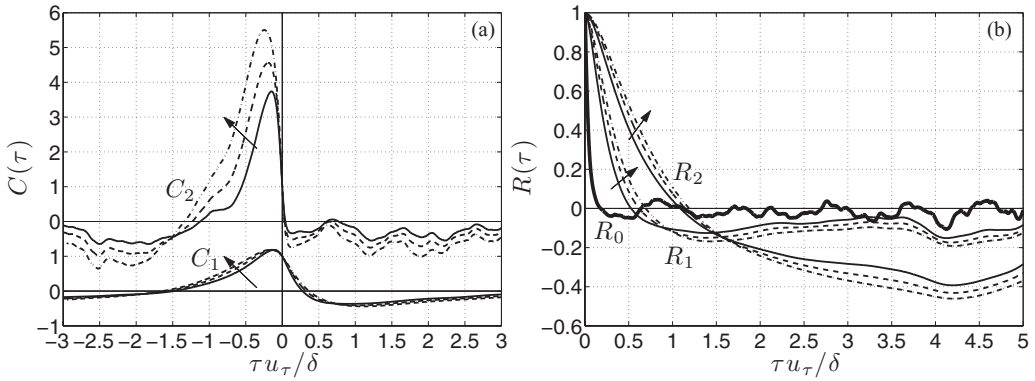


FIG. 6. Time cross-correlations $C_1(\tau)$ and $C_2(\tau)$ (shifted by 2 for clarity) (a) and auto-correlation functions (b) $R_0(\tau)$, $R_1(\tau)$, and $R_2(\tau)$ for $Re_\tau = 400$ and $\chi^* = 100$ mg l$^{-1}$; $Sc = 400$ (———), $Sc = 690$ (– – –) , $Sc = 1020$ (— · —) (trend shown by arrow).

The three signals shown in Figure 5 exhibit three visibly distinct characteristic time scales. This is confirmed by the time autocorrelations (Figure 6(b)),

$$R_0(\tau) = \frac{\langle \tau_w'(x,z;t+\tau)\tau_w'(x,z;t)\rangle}{\langle \tau_w'\tau_w'\rangle}, \tag{14}$$

$$R_1(\tau) = \frac{\langle J_{swi}'(x,z;t+\tau)J_{swi}'(x,z;t)\rangle}{\langle J_{swi}'J_{swi}'\rangle}, \tag{15}$$

$$R_2(\tau) = \frac{\langle c_{swi}'(x,z;t+\tau)c_{swi}'(x,z;t)\rangle}{\langle c_{swi}'c_{swi}'\rangle}, \tag{16}$$

where the integral time scales of $J_{swi}$ and $c_{swi}$ are more than an order of magnitude longer than the ones associated with $\tau_w$. Increasing $Sc$ results in a slower response of the diffusive sublayer and oxygen concentration in the sediment layer to the overlying turbulent forcing. The effects of $Sc$ are not visible to the same extent in spatial correlations of the same instantaneous quantities (not shown).

### C. The spatial structure of the near-wall transport

The streamwise autocorrelation functions (Figure 7)

$$R_0(\Delta x) = \frac{\langle \tau_w'(x+\Delta x,z;t)\tau_w'(x,z;t)\rangle}{\langle \tau_w'\tau_w'\rangle}, \tag{17}$$

$$R_1(\Delta x) = \frac{\langle J_{swi}'(x+\Delta x,z;t)J_{swi}'(x,z;t)\rangle}{\langle J_{swi}'J_{swi}'\rangle}, \tag{18}$$

$$R_2(\Delta x) = \frac{\langle c_{swi}'(x+\Delta x,z;t)c_{swi}'(x,z;t)\rangle}{\langle c_{swi}'c_{swi}'\rangle}, \tag{19}$$

are consistent with the considerations made in Sec. IV B. The concentration fluctuations at the SWI exhibit an extended streamwise coherence that required a longer computational domain (Table II) in that direction. The instantaneous mass flux exhibits shorter length scales in the streamwise direction with respect to the scalar concentration; however, as $Re_\tau$ increases, the characteristic streamwise

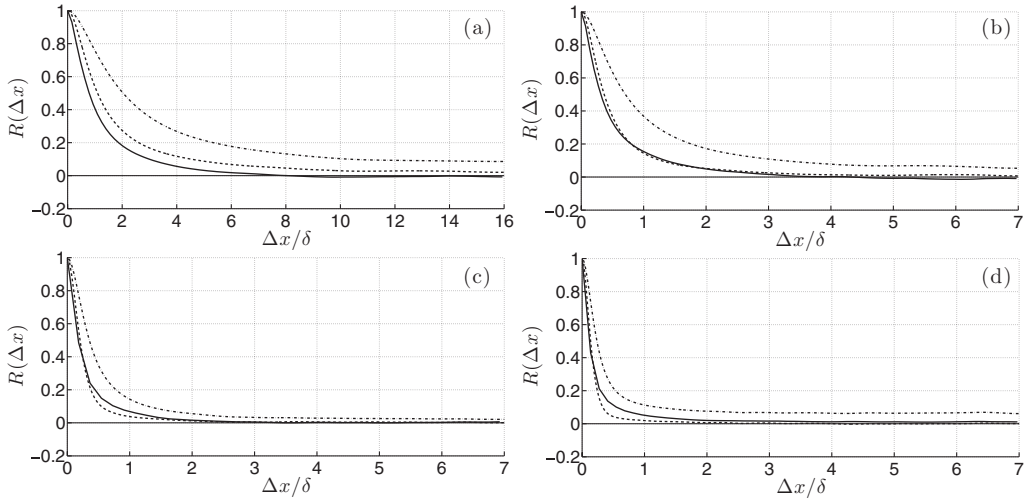


FIG. 7. Streamwise autocorrelation functions $R_0(\Delta x)$ (———), $R_1(\Delta x)$ (– – –), and $R_2(\Delta x)$ (— · —); for $Sc = 400$ and $\chi^* = 100$ mg l$^{-1}$; $Re_\tau = 180$, (*a*), $Re_\tau = 400$ (b), $Re_\tau = 620$ (c), and $Re_\tau = 1000$ (d).

extension of patches of $J_{swi}$ is systematically reduced, falling below the wall-shear-stress integral length scale. This is confirmed by experimental observations for higher Reynolds numbers.[7] We speculate that this behaviour is the sign of the diffusive sublayer becoming gradually thinner with respect to the viscous sublayer as $Re_\tau$ increases: eddies penetrate, on average, less frequently into the thinner diffusive sublayer, therefore, not sustaining the streamwise extension of patches of positive mass flux fluctuation (see discussion in Sec. V).

Increasing Schmidt numbers determine a more elongated structure of the concentration field at the SWI, consistently with the trend observed in Figure 6 and the conceptual model for the transport developed in the following. However, the effects on the spatial correlations are very minimal (not shown) and are particularly visible only for the $Re_\tau = 180$ case and for the autocorrelation of $c_{swi}$. The spatial structure of mass flux at the SWI is, in fact, determined by the velocity field. It exhibits similar characteristic length scales (Figure 7) but significantly longer time scales (Figure 6), therefore, is adequately resolved in the streamwise direction and time. The fluctuating scalar concentration field (in the case of oxygen transfer to a sediment bed) exhibits even less constraining resolution requirements.

The unresolved sub-Kolmogorov scales are not expected to have a significant influence on the correlations and spectra in the near-wall region ($y^+ < 5$), as shown in Bergant and Tiselj,[18] and even more so at $y^+ = 0$. The predicted correlations are consistent with the pipe flow experiments by Sirkar and Hanratty[7] who estimated the streamwise extension of the fluctuating mass flux at the wall and wall-shear stress to be, respectively, $350^+$ and $480^+$, with characteristic time scales of approximately $125^+$ ($=125/Re_\tau\ \delta/u_\tau$). This is consistent with all the correlations shown in Figures 6 and 7 (in particular, for the higher Reynolds numbers cases) and others, not shown, for higher Schmidt numbers.

The same spatial correlations for the mass flux in the spanwise directions (not shown) reveal shorter characteristic length scales than the wall-shear stress fluctuations, as also appreciable in the instantaneous visualizations in Figures 9 and 10. Sirkar and Hanratty[7] estimate a spanwise length scale for the mass flux and wall-shear stress fluctuations of $\sim 7^+$ and $\sim 12^+$, respectively, which is confirmed in our simulations. This is a consequence of the very high-Schmidt-number and makes a DNS resolution for the velocity field marginal for the full resolution of the scalar field in the near-wall region. The spanwise length scales of the scalar field are dictated by the spacing between the impingement regions between counter rotating streamwise vortices governing the transport in the near-wall region.[7,33]

## V. A CONCEPTUAL MODEL FOR THE TRANSPORT

Figures 8(a)–8(h) illustrate a conceptual model for the transport that can be extracted from the results shown so far. We have shown that the mass transfer is initiated by the stronger sweeps, those that penetrate deeper into the viscous sublayer and control the instantaneous diffusive sublayer thickness, and, therefore, the flux to the sediment layer. In this section we want to idealize the different stages of the mass transfer across the SWI following a significant bursting event.

During a sweep (Figure 8(a)) a patch of positive wall-shear-stress fluctuation (statistically correlated with a negative fluctuation in the wall-normal velocity above) is created at the wall. If the inertia of the high-momentum fluid particles is sufficiently high, these will carry high concentration values through the viscous sublayer, and down towards the edge of the diffusive sublayer (Figure 8(b)), where a diffusive front (headed towards the wall) is created.

The local peak in the wall-shear stress thus created is, therefore, followed by an increase of the mass flux, after, on average, a delay of $\sim 0.1\ \delta/u_\tau$ or large-eddy turnover times (LETOTs) (Figures 6(a) and 8(c)). As a result, patches of high wall-shear stress precede, in the direction of the mean flow, those of positive mass flux which persist at the SWI given their longer characteristics time scales (Figure 6(b)). The same mechanism is observed by Hasegawa and Kasagi[21] for lower Reynolds and Schmidt numbers, and Dirichlet boundary conditions of the scalar field at the wall. For higher Reynolds numbers we expect the delay to be reduced, as the extension of these patches approaches those of the wall-shear stress, as suggested by the streamwise auto-correlation functions (Figure 7) and observed in previous studies.[7]

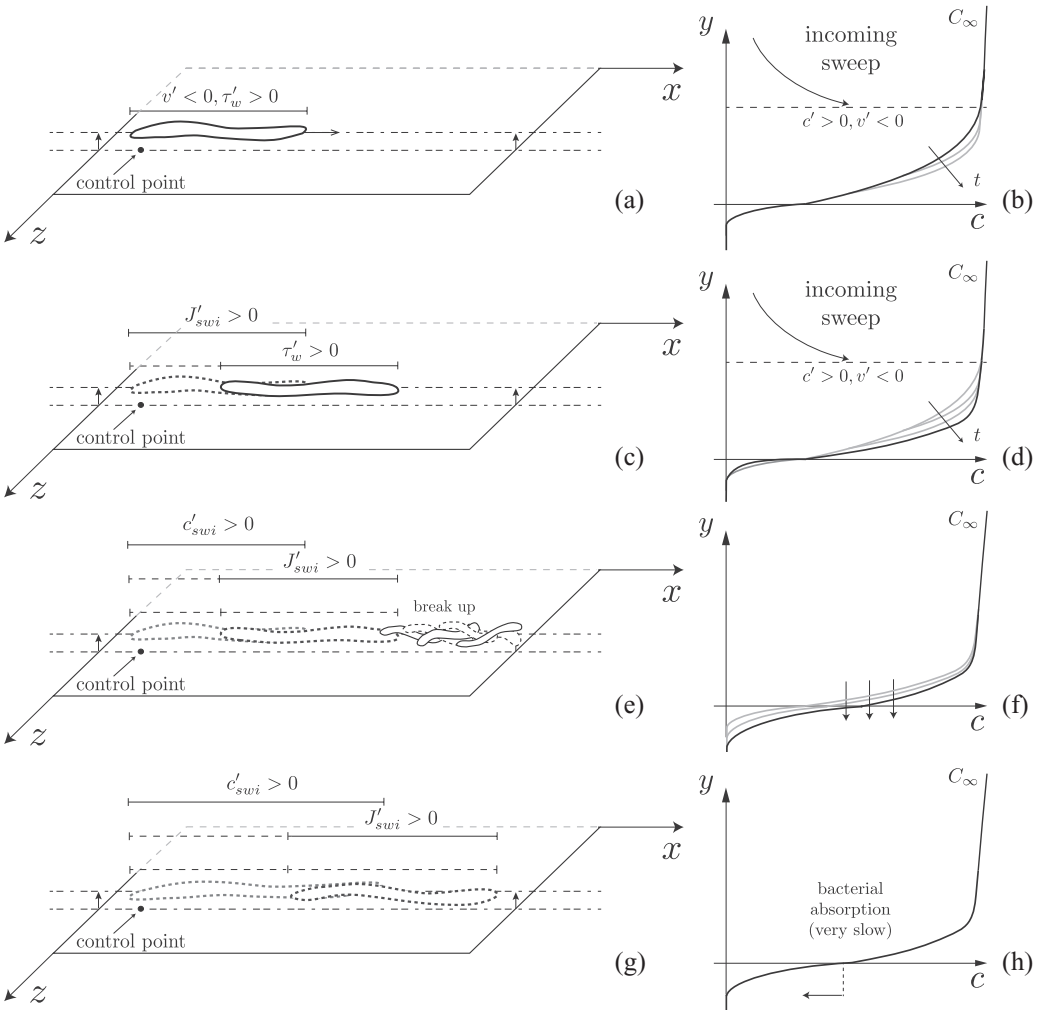


FIG. 8. Illustration of a conceptual model for the DO transfer from a turbulent flow to underlying absorbing sediment layers; generation of a high-speed streak (close to the wall) associated with a positive fluctuation of DO at the edge of the diffusive sublayer (a), (b), creation of a patch at the SWI of above-average mass flux and correspondent thinning of the diffusive sublayer (mass transfer enhancement) (c), (d), creation of an elongated patch at the SWI of above-average DO concentration and local relaxation of the mass flux (e), (f), slow bacterial absorption of the excess DO transferred across the SWI (g), (h); Figures (b), (d), (f),(h) correspond to concentration profiles as observed from the respective control points in Figures (a), (c), (e), (g).

At this stage the diffusive flux at the control point has been enhanced (Figure 8(d)), patches of positive wall-shear stress have rapidly disappeared due to instabilities (Figure 8(e)) and transfer across the SWI will occur (Figure 8(f)). However, given the extremely low diffusivity there will be a time lag between positive fluctuations in the flux and the corresponding increase in the concentration (Figure 6(a)). The result is a prolonged streamwise extensions of these patches (with respect to the overlying turbulent structures) whose persistence at the SWI is allowed by the long time scales of bacterial absorption. This leads to the final state shown in Figure 8(g) where patches of high wall-flux, preceding patches of above-average oxygen concentration at the SWI, persist at the interface in locations where rapidly evolving high speed streaks have, previously, reached the maximum intensity.

Instantaneous visualizations (Figure 9) confirm the dynamics of transport explained above. The mass transfer is initiated by strong bursting events, such as the positive fluctuation patch of $\tau_w$ initially located at $x = 2.3$, $z = 0.7$ at time $t = 0$ (transport event shown by a black arrow). There are no simultaneous traces of this event in the mass flux distribution or the concentration contours. After

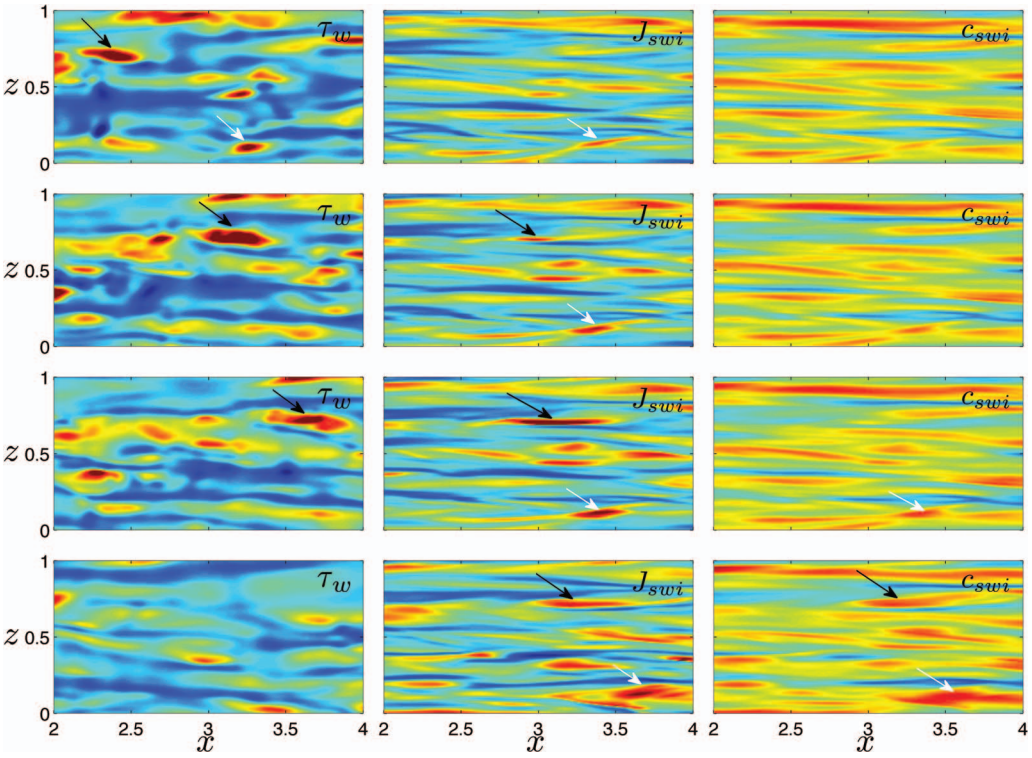


FIG. 9. Contours of instantaneous wall-shear stress $\tau_w$ (left), mass flux at SWI $J_{swi}$ (middle) and DO concentration at SWI $c_{swi}$ (right) for $Re_\tau = 400$, $Sc = 400$, and $\chi^* = 100\,\mathrm{mg\,l^{-1}}$. Initial time $t = 0$ (top row), $t = 0.056\,\delta/u_\tau$ (second row), $t = 0.095\,\delta/u_\tau$ (third row), and $t = 0.311\,\delta/u_\tau$ (forth row). Black and white arrows highlight different transport events like the one described in Figure 8.

some time, at $t = 0.056\,\delta/u_\tau$, the quickly evolving patch has reached the location $x = 3.2$ leaving behind a first trace of above-average mass flux starting to appear at $x = 2.9$. After $\Delta t = 0.0388\,\delta/u_\tau$, at time $t = 0.095\,\delta/u_\tau$, the high-speed streak starts to break up due to instabilities; on the other hand, the above-average mass flux patch is still developing (primarily) in the streamwise direction. At this stage the above-average DO concentration patch has not yet appeared; in this case, it will take another $\Delta t = 0.215\,\delta/u_\tau$ (arriving at time $t = 0.311\,\delta/u_\tau$) for it to be visible reaching its peak when the mass flux in that region is starting to relax. The same description also applies to the transport event indicated by the white arrow which is, however, captured here at a later stage of evolution.

In additional multimedia material (Figure 10, Video 1) we show how intense bursting events periodically "scar" the diffusive sublayer, sustaining a statistically steady mass transfer. It is possible to appreciate the long time scales and the slow response of the diffusive sublayer to the overlying turbulence; this is the reason why the scalar field, in high-Schimdt-number mass-transfer simulations, takes considerably longer to reach a statistical steady state than the velocity field for the same flow as also pointed out by Bergant and Tiselj.[18] It is also shown how subsequent, but completely uncorrelated bursting events, occurring on the same location on the SWI, can prolong the spatial extension and the residence time of the same above-average patch of mass-flux developing there. A similar event is shown in Figure 5 where an above-average value of the mass flux, at the same location on the SWI, is sustained from $t = 1.8\,\delta/u_\tau$ to $t = 3.3\,\delta/u_\tau$ by subsequent peaks in the wall-shear stress. If bursting events affect the diffusive sublayer less frequently (due, for example, to the thinning of the diffusive sublayer with respect to the viscous sublayer) the streamwise extension of patches of mass flux will not be sustained to the same extent (see discussion in Sec. IV C).

Additional simulations have been carried out with constant Neumann and Dirichlet boundary conditions (with no sediment layer), matching, respectively, the average gradient and average DO concentration at the SWI for case $Sc = 400$ and $Re_\tau = 400$. Temporal correlations at the wall

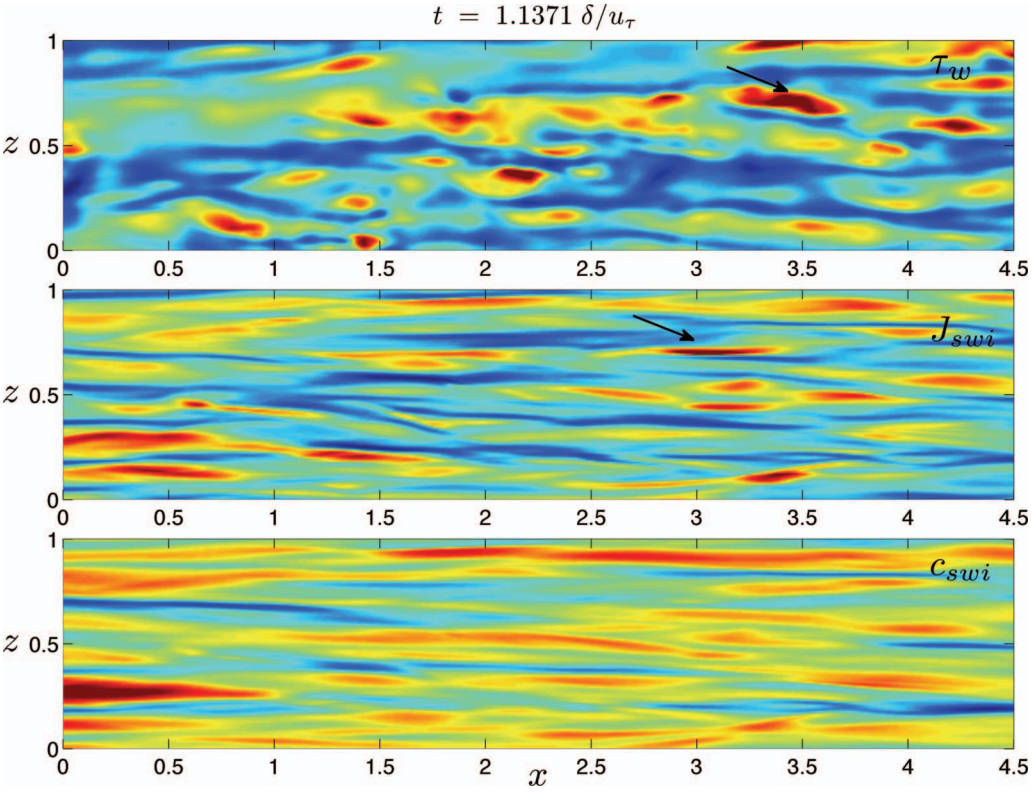


FIG. 10. Flow animation showing instantaneous wall-shear stress, $\tau_w$ (top), mass flux at the SWI, $J_{swi}$ (middle), and oxygen concentration at the SWI, $c_{swi}$ (bottom) for $Re_\tau = 400$, $Sc = 400$, and $\chi^* = 100\,\text{mg}\ 1^{-1}$ (enhanced online) [URL: http://dx.doi.org/10.1063/1.4739064.1].

(not shown) reveal a similar relationship between $\tau_w$ and $J_{swi}$ (for constant Dirichlet boundary conditions or constant $c_{swi}$) and between $\tau_w$ and $c_{swi}$ (for constant Neumann boundary conditions or constant $J_{swi}$). This suggests that the transport mechanisms described in the present work can be extended to high-Schmidt-number mass transfer in general and are also valid for lower Schmidt numbers.[21] The effects on the turbulent transport dynamics of the absorbing sediment layer are, however, still visible but limited to the diffusive sublayer. In presence of an active sediment layer, temporal cross-correlations between $\tau_w$ and $c_{swi}$ reveal almost no correlation for zero separation in time. The instantaneous concentration at the SWI is not immediately affected by the overlying turbulence due to the inertia of the diffusive sublayer. On the other hand, for example, simulations with constant (instantaneous) scalar flux at the wall, cause every location of the diffusive sublayer to be synchronized and therefore, the concentration value at the wall, to retain a finite and positive correlation with the wall-shear stress for zero separation in time. This is also corroborated by the fact that RMS profiles of scalar concentration, in the case of Neumann boundary conditions, are constant throughout the diffusive sublayer thickness.

## VI. CONCLUSIONS

We have investigated the mechanisms involved in oxygen depletion by smooth organic sediment layers interacting with a turbulent flow with focus on the mass transport occurring across the SWI. Statistically steady oxygen depletion has been simulated for different combinations of $Sc$, $Re_\tau$, and $\chi^*$ over typical lab-scale ranges in an open-channel configuration.

The average sediment-oxygen uptake varies with $Sc$ and $Re_\tau$ in good agreement with classic heat-and-mass-transfer laws. The analysis of the instantaneous wall-shear-stress distribution, mass flux, and DO concentration at the SWI has allowed for the extraction of a conceptual model for the

transport which encompasses and extends many fundamental ideas on high-Schmidt-number mass transfer present in previous work. The complexity of the diffusive sublayer nature emerging from this analysis goes beyond the classic low-pass filter characterization, it also includes de-noising and amplitude filtering properties: the diffusive sublayer thickness or, equivalently, the mass flux at the wall, is modulated primarily by the intense sweeps (amplitude filter), it is not responsive to low-amplitude background fluctuations of the wall-shear stress (de-noising filter) and it exhibits an integral response to the forcing (low-pass filter) with a response delayed by fractions of an LETOT. The sediment layer oxygen content also exhibits a smoother and delayed response to the variable mass flux at the interface. The overall picture arising from this analysis of oxygen depletion identifies three distinct transport processes: turbulent transport within the viscous sublayer, molecular mass transport across the diffusive sublayer and transport within the sediment layer. Each of these processes exhibits distinct time and spatial scales and are connected through a well-defined cause-and-effect relationship.

The extracted transport model stresses the intrinsic unsteady and three-dimensional nature of the mass transport at the wall which should not be ignored when formulating semi-analytical models for the near-wall transport. The overall picture arising confirms the fundamental ideas at the basis of the surface-renewal theory brought forward by Hanratty[4] and Pinczewski and Sideman.[8]

## ACKNOWLEDGMENTS

The authors acknowledge the financial support of the Natural Science and Engineering Research Council of Canada under the Discovery Grant Program and the Canada Research Chair program. The authors also thank the High Performance Computing Virtual Laboratory (HPCVL), Queen's University site, for the computational support.

[1] A. Fage and H. C. H. Townend, "An examination of turbulent flow with an ultramicroscope," Proc. R. Soc. London, Ser. A **135**, 656–677 (1932).
[2] C. S. Lin, R. W. Moulton, and G. L. Putnam, "Mass transfer between solid wall and fluid streams. Mechanism and eddy distribution relationships in turbulent flow," Ind. Eng. Chem. **45**, 636–640 (1953).
[3] H. A. Einstein and H. Li, "The viscous sublayer along a smooth boundary," J. Eng. Mech. **82**(2), 1–7 (1956).
[4] T. J. Hanratty, "Turbulent exchange of mass and momentum with a boundary," AIChE J. **2**, 359–362 (1956).
[5] B. P. Boudreau and B. B. Jørgensen, *The Benthic Boundary Layer: Transport Processes and Biogeochemistry* (Oxford University Press, New York, 2001).
[6] L. P. Reiss and T. J. Hanratty, "Measurement of instantaneous rates of mass transfer to a small sink on a wall," AIChE J. **8**, 245–247 (1962).
[7] K. K. Sirkar and T. J. Hanratty, "Relation of turbulent mass transfer to a wall at high Schmidt numbers to the velocity field," J. Fluid Mech. **44**, 589–603 (1970).
[8] W. V. Pinczewski and S. Sideman, "A model for mass (heat) transfer in turbulent tube flow. Moderate and high Schmidt (Prandtl) numbers," Chem. Eng. Sci. **29**, 1969–1976 (1974).
[9] D. A. Shaw and T. J. Hanratty, "Influence of Schmidt number on the fluctuations of turbulent mass transfer to a wall," AIChE J. **23**, 160–169 (1977).
[10] P. V. Shaw and T. J. Hanratty, "Fluctuations in the local rate of turbulent mass transfer to a pipe wall," AIChE J. **10**, 475–482 (1964).
[11] J. A. Campbell and T. J. Hanratty, "Turbulent velocity fluctuations that control mass transfer to a solid boundary," AIChE J. **29**, 215–221 (1983).
[12] J. A. Campbell and T. J. Hanratty, "Mechanism of turbulent mass transfer at a solid boundary," AIChE J. **29**, 221–229 (1983).
[13] J. A. Campbell, "The velocity-concentration relationship in turbulent mass transfer to a wall," Ph.D. dissertation (University of Illinois, Urbana, 1981).
[14] H. Røy, M. Huettel, and B. B. Jørgensen, "Transmission of oxygen concentration fluctuations through the diffusive boundary layer overlying aquatic sediments," Limnol. Oceanogr. **49**, 686–692 (2004).
[15] B. L. O'Connor and M. Hondzo, "Dissolved oxygen transfer to sediments by sweep and eject motions in aquatic environments," Limnol. Oceanogr. **53**, 566–578 (2008).
[16] I. Calmet and J. Magnaudet, "Large-eddy simulation of high-Schmidt-number mass transfer in a turbulent channel flow," Phys. Fluids **9**, 438 (1997).
[17] Y. H. Dong, X. Y. Lu, and L. X. Zhuang, "Large eddy simulation of turbulent channel flow with mass transfer at high-Schmidt numbers," Int. J. Heat Mass Transfer **46**, 1529–1539 (2003).
[18] R. Bergant and I. Tiselj, "Near-wall passive scalar transport at high Prandtl numbers," Phys. Fluids **19**, 065105 (2007).
[19] C. Scalo, U. Piomelli, and L. Boegman, "Large-eddy simulation of oxygen transfer to organic sediment beds," J. Geophys. Res. **117**, C06005, doi:10.1029/2011JC007289 (2012).

[20] F. Schwertfirm and M. Manhart, "DNS of passive scalar transport in turbulent channel flow at high Schmidt numbers," Int. J. Heat Fluid Flow **28**, 1204–1214 (2007).
[21] Y. Hasegawa and N. Kasagi, "Low-pass filtering effects of viscous sublayer on high schmidt number mass transfer close to a solid wall," Int. J. Heat Fluid Flow **30**, 525–533 (2009).
[22] M. Higashino, B. L. O'Connor, M. Hondzo, and H. G. Stefan, "Oxygen transfer from flowing water to microbes in an organic sediment bed," Hydrobiologia **614**, 219–231 (2008).
[23] B. L. O'Connor and M. Hondzo, "Enhancement and inhibition of denitrification by fluid-flow and dissolved oxygen flux to stream sediments," Environ. Sci. Technol. **42**, 119–125 (2007).
[24] M. Higashino, J. J. Clark, and H. G. Stefan, "Pore water flow due to near-bed turbulence and associated solute transfer in a stream or lake sediment bed," Water Resour. Res. **45**, W12414, doi:10.1029/2008WR007374 (2009).
[25] M. Higashino and H. G. Stefan, "Dissolved oxygen demand at the sediment-water interface of a stream: Near-bed turbulence and pore water flow effects," J. Environ. Eng. **137**, 531 (2011).
[26] M. Higashino and H. Stefan, "Model of turbulence penetration into a suspension layer on a sediment bed and effect on vertical solute transfer," Environ. Fluid Mech. 1–19 (2012).
[27] A. Lorke, B. Müller, M. Maerki, and A. Wüest, "Breathing sediments: The control of diffusive transport across the sediment-water interface by periodic boundary-layer turbulence," Limnol. Oceanogr. **48**, 2077–2085 (2003).
[28] A. Leonard, "Energy cascade in large-eddy simulations of turbulent fluid flows," Adv. Geophys. **18**, 237–248 (1974).
[29] M. Germano, U. Piomelli, P. Moin, and W. H. Cabot, "A dynamic subgrid-scale eddy viscosity model," Phys. Fluids A **3**, 1760–1765 (1991).
[30] D. K. Lilly, "A proposed modification of the Germano subgrid-scale closure method," Phys. Fluids A **4**, 633–635 (1992).
[31] A. Keating, U. Piomelli, K. Bremhorst, and S. Nešić, "Large-eddy simulation of heat transfer downstream of a backward-facing step," J. Turbul. **5**, 1–27 (2004).
[32] D. A. Shaw and T. J. Hanratty, "Turbulent mass transfer to a wall for large Schmidt numbers," AIChE J. **23**, 28–37 (1977).
[33] J. Jimenez and A. Pinelli, "The autonomous cycle of near-wall turbulence," J. Fluid Mech. **389**, 335–359 (1999).